Forced ignition of premixed cool and hot DME/air flames in a laminar counterflow

Yan Wang[1], Shumeng Xie[1, 3], Hannes Böttler[2], Yiqing Wang[1], Xinyi Chen[2], Arne Scholtissek[2], Christian Hasse[2], Zheng Chen[1,*]

[1] HEDPS, SKLTCS, CAPT, College of Engineering, Peking University, Beijing, 100871, China

[2] Department of Mechanical Engineering, Simulation of reactive Thermo-Fluid Systems, Technical University of Darmstadt, Otto-Berndt-Str. 2, 64287 Darmstadt, Germany

[3] Department of Mechanical Engineering, National University of Singapore, 9 Engineering Drive 1, Singapore 117576, Republic of Singapore

Abstract

Recently, low-temperature chemistry (LTC) and LTC-induced cool flames have attracted extensive interest since they can substantially influence the ignition process and accelerate the subsequent hot flame propagation. However, it is unclear how the flow affects the forced ignition of a cool flame and its subsequent transition to a hot flame. In this study, we conduct transient 2D simulations for the forced ignition processes of premixed cool and hot flames in a laminar, axisymmetric, counterflow configuration with well-defined flow field. Different ignition energies and strain rates are used to ignite and stabilize cool and/or hot flames in a counterflow. The critical conditions for the ignition of cool and hot flames are identified, and the cool flame kernel quenching and its transition to hot flame are discussed. It is found that the ignition energy determines the highest temperature and thereby controls the thermal runaway process. The strain rate influences the flame kernel propagation and the transition from cool flame to hot flame. A large strain rate may quench the cool flame, while a small strain rate may lead to the transition from cool flame to hot flame due to the sufficiently long residence time. Therefore, cool flame ignition and stabilization can only be achieved within a certain range of strain rates. Furthermore, an ignition regime diagram in terms of ignition energy and strain rate is proposed, and four regimes are identified: (I) only cool flame, (II) only hot flame, (III) ignition failure, and (IV) transition from cool flame to hot flame (with appearance of double flame structure). These results provide new insights into how the flow affects the cool flame ignition and transition.

Keywords: cool flame, forced ignition, strain rate, LTC

* E-mail: cz@pku.edu.cn. Tel: 86-10-62766232.

Novelty and Significance Statement

In this study, we conduct transient 2D simulations for the forced ignition processes of premixed cool and hot flames in a laminar, axisymmetric, counterflow configuration with a well-defined flow field. To the best of authors' knowledge, this is the first numerical study that examines the flow effects on the forced ignition of cool flames and on the transition from a cool flame to a hot flame. It is demonstrated that the counterflow strain rate has a great impact on cool flame ignition and its transition to a hot flame. A novel ignition regime diagram in terms of ignition energy and strain rate (see Fig. 16) is proposed, in which four ignition regimes are identified: (I) only cool flame, (II) only hot flame, (III) ignition failure, and (IV) transition from cool flame to hot flame. This study provides new insights into how the flow affects the cool flame ignition and transition.

Authors Contributions

Conceptualization, Y.W., S.X. and C.Z.; methodology and formal analysis, Y.W. and S.X.; assisted in further analysis, H.B., Y.W., X.C. and A.S.; writing—original draft, Y.W. and S.X.; writing—review and editing, H.B., Y.W., X.C., A.S., C.H. and Z.C.; supervision and project administration, C.H. and Z.C. All authors have read and agreed to the final version of the manuscript.

1 Introduction

A cool flame can be observed during the combustion of large hydrocarbon fuels [1, 2]. It is controlled by the low-temperature chemistry (LTC) [3] and is closely related to the two-stage ignition behavior, which results in the negative temperature coefficient (NTC) phenomenon [4]. Recently, the cool flame has attracted wide attention due to its important role in high-pressure and low-temperature combustion in advanced engines [5, 6], such as homogeneous charge compression ignition (HCCI) engines and spark assistant compression ignition (SACI) engines. A lot of experimental and numerical studies have been conducted for cool flames, including cool flames in droplet combustion under microgravity [7], spherically propagating cool flames [8, 9], cool flames in a counterflow configuration [10-12], and cool flames in temperature-controlled micro-reactors [13]. These studies mainly focused on the flame speed, flammability limit, extinction/ignition limit, and transition between cool and hot flames.

However, there are only a few studies on the forced ignition of cool flames. The critical ignition conditions for cool flames are still not fully understood, which motivates the present study. Zhang et al. [14] investigated the transient evolution of a cool flame ignited by a hot spot and found that the cool flame ignition is greatly affected by the hot spot temperature and size. Yang and Zhao [15]

computed the minimum ignition energy (MIE) for cool and hot flames and found that the cool flame has a lower MIE and a wider flammability range than the hot flame. Wang et al. [16] explored the premixed cool ignition induced by a hot particle. Their results indicate that the LTC can substantially promote the ignition process. Wang et al. [17] investigated the forced ignition process in the mixing layer and observed that the cool, warm and hot flames can be initiated sequentially, resulting in a penta-brachial flame structure consisting of a trailing warm flame and a trailing cool flame attached to the hot triple flame. These studies show that the LTC-induced cool flame can substantially reduce the ignition energy and accelerate the subsequent hot flame development. Most of these studies considered static mixtures. However, practical ignition usually occurs in flowing environments and the flow may affect the cool flame ignition through convective transport of mass and heat.

There are ample evidences indicating that the flow has a significant impact on the forced ignition of premixed flames. Baum and Poinsot [18] demonstrated via 2D simulations that the minimal ignition power increases nearly linearly with the flow speed. Beduneau et al. [19] conducted laser ignition experiments for methane/air mixtures and observed that the MIE increases and decreases with flow velocity for fuel-rich and fuel-lean cases, respectively. Kobayashi et al. [19] conducted laser-induced ignition experiments in dimethyl ether/air mixtures and found that the MIE first decreases and then increases with the flow velocity. Xie et al. [20] simulated the forced ignition process in a counter-flowing H_2/air mixture and found that the coupling between Lewis number and stretch rate greatly affects the ignition kernel development. Moreover, the counterintuitive turbulence-facilitated ignition ([21] and references therein) and flow-facilitated ignition [22] have been observed in recent experiments and simulations, respectively. However, these studies only considered the flow effects on the forced ignition of premixed hot flames. It is still unclear how the flow affects cool flame ignition.

Based on the aforementioned considerations, this study aims to numerically assess the flow effects on the ignition of a premixed cool flame and its subsequent transition to a hot flame. We consider the forced ignition of premixed DME/air in a 2D, laminar, axisymmetric counterflow configuration with a well-defined flow field. Different ignition energies and strain rates are considered so that cool and/or hot flames can be ignited and stabilized in a counterflow. The remainder of the paper is structured as follows. In Section 2, the model and numerical specifications are described. Section 3 presents the results from numerical simulations. First, the ignition and propagation of cool flame is studied. Then, the effects of ignition energy and strain rate on cool ignition are assessed. Finally, an ignition regime diagram in terms of ignition energy and strain rate is proposed. Section 4 outlines the main conclusions.

2 Model and numerical specifications

We consider the transient forced ignition process in a 2D axisymmetric counterflow as shown in Fig. 1. A stoichiometric DME/air mixture is injected from the upper and lower boundaries with a uniform inlet velocity denoted by U_{in}. The global strain rate of the counterflow is $a_g = 4U_{\text{in}}/L$ [23], where L is the distance between two inlet nozzles. The DME/air mixture is at an elevated temperature and pressure of T_u = 450 K and P = 5 atm. At this thermal state, the cool flame can be ignited and the second-stage autoignition inducing the transition from a cool flame to a hot flame is not very long, which helps to reduce the computational cost.

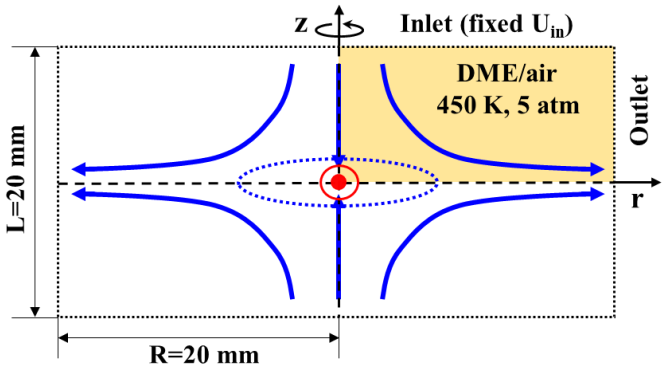

Fig. 1. Schematic of the forced ignition in a 2D axisymmetric counterflow. The computation domain is highlighted in yellow.

Due to symmetry, the computation domain is reduced to the red region in Fig. 1, whose size is 20×10 mm^2. On the left and bottom sides, symmetric boundary conditions are used. The pressure outlet boundary is applied on the right side, while a uniform inlet flow is imposed on the top side. To ensure grid convergence, a uniform mesh with Δr=Δz=25 μm is employed and the reaction zone is always covered by more than 20 grid points.

Before ignition, the mixture is frozen and the steady counterflow is calculated and used as the initial condition. The center of the ignition kernel is set at the stagnation point (r=z=0). The mixture is ignited by adding the following source term $\dot{q}$ in the energy equation:

$$\dot{q} = \frac{3E_{\text{ign}}}{4\pi R_{\text{ign}}^3 \tau_{\text{ign}}} \exp\left(-\frac{\pi}{4}\left(\frac{r^2+z^2}{R_{\text{ign}}^2}\right)^3\right)\left(H\left(t-\tau_{\text{ign}}\right) - H(t)\right) \quad (1)$$

where E_{ign} is the total ignition energy, R_{ign} is the radius of energy deposition region, τ_{ign} is the duration of energy deposition, and $H(t)$ is the Heaviside function. Here we choose fixed values of R_{ign} = 500 μm and τ_{ign} = 200 μs. Note that the ignition is quantitatively affected by R_{ign} and τ_{ign} [24], but the main conclusions are independent of the values of R_{ign} and τ_{ign}.

The transient ignition and flame propagation/stabilization processes are simulated using the OpenFOAM-based EBI-DNS solver developed by Zirwes et al. [25-27]. The governing equations for compressible reactive flow are solved using the finite volume method. Details on the governing equations and numerical schemes can be found in [25] and thereby are not repeated here. Cantera [18] is incorporated into EBI-DNS to evaluate the reaction rates as well as thermal and transport properties. The mixture-averaged transport model is applied to compute the diffusion velocity. This code has been widely validated and used in the simulations of ignition and flame propagation [16, 17, 20, 28, 29]. A skeletal mechanism consisting of 39 species and 175 reactions [30] is used in simulations. This mechanism includes both LTC and high-temperature chemistry (HTC), and it has been frequently used in previous cool flame studies [14, 16, 17]. Note that radiation heat loss has negligible influence on cool flame and thereby is not considered here.

3 Results and discussion

In this paper, the ignition processes at different strain rates a_g and different ignition energies E_{ign} are investigated. Five typical combinations of strain rate and ignition energy are listed in the insert in Fig. 2, which also shows the maximum flame temperature over time for all cases. Case A with a_g = 40 s^{-1} and E_{ign} = 0.825 mJ corresponds to the ignition of a cool flame. The cool flame kernel propagates outward and eventually evolves into a steady counterflow cool flame whose flame temperature is around 800 K. Compared to case A, case B has a higher ignition energy of E_{ign} = 1.25 mJ while the same strain rate of a_g = 40 s^{-1} is imposed. The increase in ignition energy directly induces the HTC reactions. Subsequently, a hot flame with temperature exceeding 2300 K is ignited for case B as shown in Fig. 2. On the contrary when the ignition energy is reduced to E_{ign} = 0.625 mJ for case C, no thermal runaway is triggered, resulting in ignition failure. Figure 2 shows that the maximum temperature gradually decays to the ambient temperature of 450 K for case C.

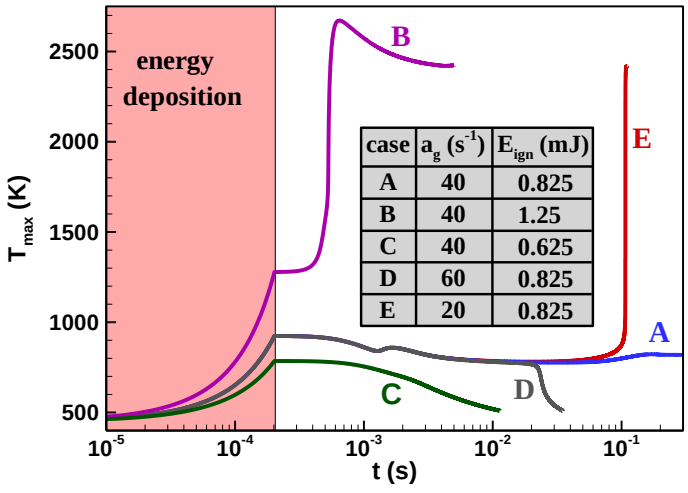

Fig. 2. Temporal evolutions of the maximum temperature T_{max} for five typical ignition processes

with different ignition energies and global strain rates.

Cases D and E have the same ignition energy as case A, but have a higher and lower strain rate, respectively. When the strain rate is increased to $a_g = 60$ s^{-1} for case D, the cool flame ignition kernel quenches as it travels along the stagnation plane. Figure 2 shows that the maximum temperature for case D suddenly drops at around $t = 0.03$ s when flame quenching happens. On the contrary, when the strain rate is reduced to $a_g = 20$ s^{-1} for case E, the intermediate species produced by the cool flame experience sufficient residence time to undergo high-temperature chemical reactions, leading to the formation of a hot flame. The maximum flame temperature is shown to reach 2300 K at around $t = 0.1$ s when the hot flame appears.

In the following, we first analyze the cool flame ignition and propagation for case A in Section 3.1. Then, the ignition processes for different ignition energies corresponding to the cases A, B, and C are discussed in Section 3.2. The cool flame quenching and its transition to the hot flame under different strain rates for cases A, D, and E are investigated in Section 3.3. Finally, the ignition regime diagram for cool and hot flames is summarized in Section 3.4.

3.1 Cool flame ignition and propagation

In this subsection, we only consider the cool flame ignition and propagation for case A with $a_g = 40$ s^{-1} and $E_{ign} = 0.825$ mJ.

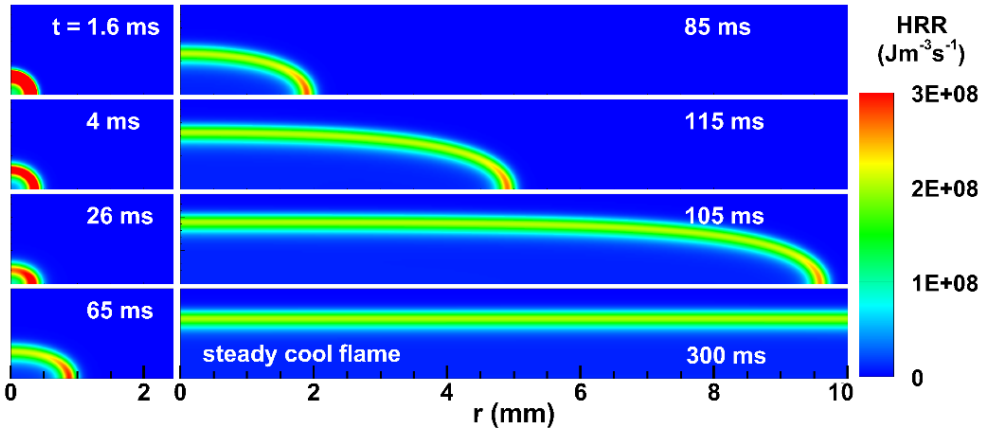

Fig. 3. Evolution of heat release rate (HRR) during the cool flame ignition and propagation for case A. The height for each sub-figure is 1.35 mm. An animation is provided in the Supplementary Material.

The evolution of the heat release rate (HRR) distribution is shown in Fig. 3. After the thermal runaway, a cool flame kernel is formed. During the initial period from 0 to 4 ms, the outward propagation of the cool flame kernel is mainly driven by the ignition energy deposition. Then during

t = 4~26 ms, the effect of ignition energy deposition diminishes, and the flame kernel shrinks in the axial direction due to the counterflow and thereby evolves into an ellipsoidal shape. After t > 26 ms, the chemically active cool flame front at z = 0.9 mm, the fuel and oxidizer are only partially consumed, and the temperature rises from 450 K to about 820 K. The intermediate species, formaldehyde (CH_2O) and hydrogen peroxide (H_2O_2), are generated by the cool flame (Fig. 4 right). At the cool flame front, a large amount of $CH_3OCH_2O_2$ is produced via the LTC reaction $CH_3OCH_3 + O_2 = CH_3OCH_2 + HO_2$. The cool flame structure is similar to that reported by Zhang et al. [14] and details on the LTC of DME can be found in [6]. Note that unlike the case of ignition in a static mixture in which the hot flame appears after the cool flame [14], here no hot flame is produced. This is because in the present counterflow with a_g = 40 s^{-1}, there is not sufficient residence time for the intermediate products to undergo the high-temperature reactions. Only for sufficiently low strain rates, the hot flame will appear after the cool flame (e.g., case E, which will be discussed extensively in subsection 3.3).

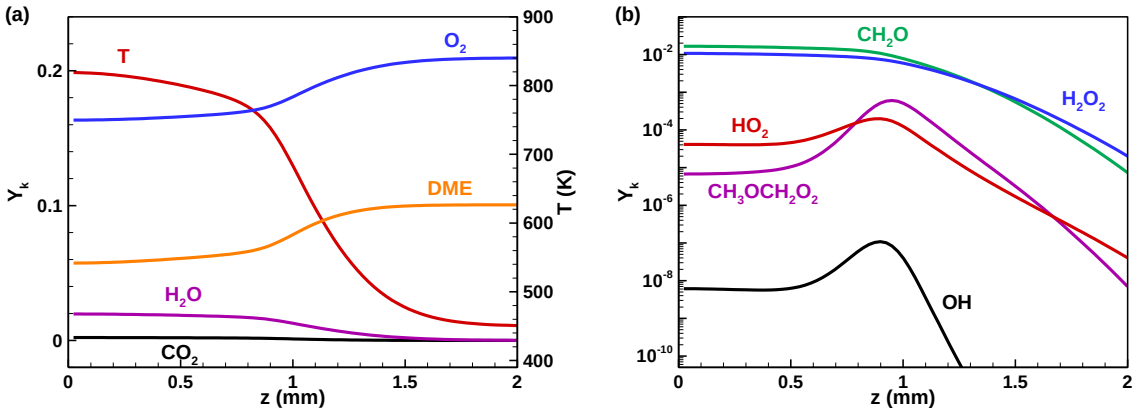

Fig. 4. The distributions of temperature and mass fractions of different species in the steady cool flame structure along the symmetry axis (i.e., r=0) for case A at t = 300 ms.

To further investigate how the ignition kernel evolves into a steady cool flame, we calculate the density weighted displacement speed S_d^* along the flame front, which is defined as [31]:

$$S_d^* = \frac{\rho S_d}{\rho_u} = \frac{\omega_{CH_2O}}{\rho_u |\nabla Y_{CH_2O}|} + \frac{\nabla \cdot (\rho D_{CH_2O} \nabla Y_{CH_2O})}{\rho_u |\nabla Y_{CH_2O}|} \quad (2)$$

where ρ is the local density, ρ_u the density of unburned mixture, S_d the displacement speed, ω_{CH2O} the chemical production rate of CH_2O, and D_{CH2O} the mass diffusivity of CH_2O, and Y_{CH2O} the mass

fraction of CH_2O. The iso-line of Y_{CH2O}=0.0095 is selected to represent the cool flame front because its position is close to the peak of the heat release rate in the unstretched planar cool flame. The local stretch rate K is calculated according to the following equation [32]:

$$K = \frac{1}{A}\frac{dA}{dt} = \nabla_{\tau} \cdot (\boldsymbol{u} + S_d \boldsymbol{n}) = (\boldsymbol{I} - \boldsymbol{nn}) : \boldsymbol{S} + S_d(\nabla \cdot \boldsymbol{n}) \quad (3)$$

where ∇_{τ} is the gradient along the flame surface in its tangential direction, $\boldsymbol{u}$ the local flow velocity, $\boldsymbol{n}$ the normal vector of the flame front, $\boldsymbol{I}$ the unit matrix, and $\boldsymbol{S}$=symm($\nabla \boldsymbol{u}$) the strain rate tensor. The first term on the right-hand side of Eq. (3) is the aerodynamic strain rate contributed by the local flow velocity, and the second term represents the contribution of flame curvature $\nabla \cdot \boldsymbol{n}$ which is positively correlated with the flame displacement speed.

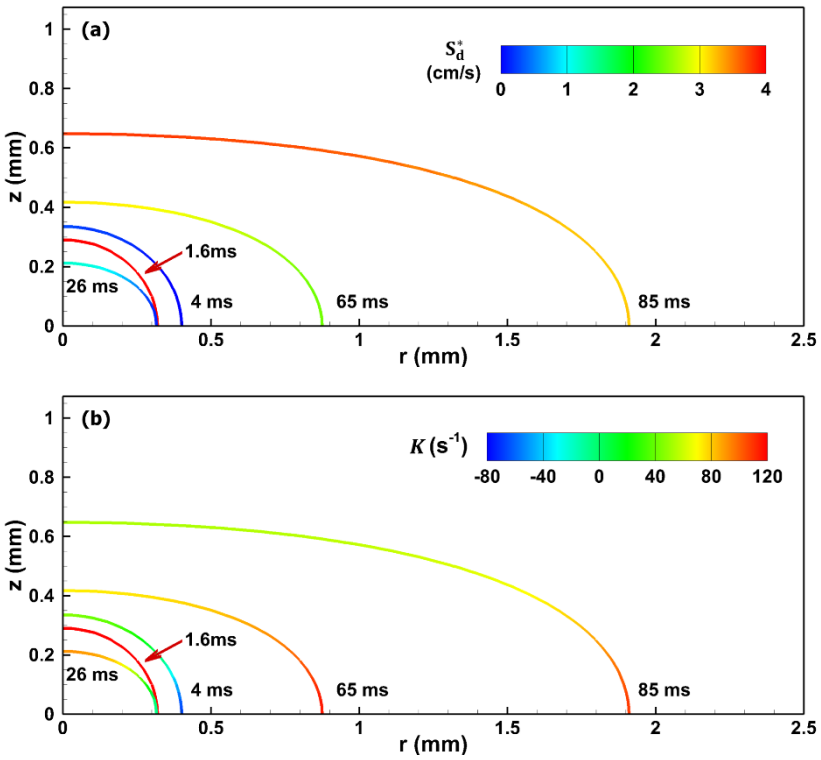

Fig. 5. Temporal evolution of (a) density weighted displacement speed S_d^* and (b) local stretch rate K along the cool flame front for case A.

Figure 5 shows the evolution of the density-weighted displacement velocity S_d^* and the local stretch rate K for case A. It is observed that S_d^* decreases rapidly from t = 1.4 ms to t= 4 ms. This is because the initial flame kernel propagation is mainly driven by the ignition energy deposition and its speed decreases greatly when there is no ignition energy deposited around the stagnation point. According to Eq. (3), the local stretch rate is proportional to S_d. Therefore, K also decreases rapidly from t = 1.4 ms to t= 4 ms. During t = 4~26 ms, the cool flame kernel shrinks under the counterflow field. However, the reaction rate of LTC starts to increase and so do the displacement speed and local

stretch rate. After t > 26 ms, S_d^* becomes larger than the local flow velocity, and thereby the cool flame propagates outward. In the axial direction (i.e., at r=0), the flame curvature gradually decreases and so does the local stretch rate. However, in the radial direction (i.e., at z=0) the flame is highly curved, and thereby K increases with S_d according to Eq. (3). For a given time of t = 65 or 85 ms, Fig. 5 shows that S_d^* and K respectively decreases and increases in the clockwise direction along the cool flame front. This is because the effective Lewis number is slightly above unity and thereby the positive stretch rate slows down the premixed flame propagation [32].

Figure 6 plots the change of density weighted displacement speed S_d^* with local stretch rate K. Similar to the expanding spherical flames reported in [33, 34], the cool flame propagation in the axial direction (i.e., r = 0) consists of three distinct regimes: spark-assisted ignition kernel propagation regime (dashed line A_zB_z in Fig.6), the unsteady flame transition regime (B_zC_z), and the quasi-steady flame propagation regime (C_zD_z). During the first regime, A_zB_z, with 0 < t < 4 ms, both S_d^* and K decrease as the cool flame kernel expands. In the second regime, B_zC_z, with 4 < t < 26 ms, the LTC reaction rate starts to increase and so do both, S_d^* and K. In the quasi-steady regime, C_zD_z, with 26 < t < 85 ms, S_d^* increases while K decreases during the cool flame propagation, resulting in a linear decrease of S_d^* with K and thereby a positive Markstein length. Results for an expanding spherical cool flame in a static mixture are also shown in Fig. 6 for comparison. A similar trend is observed between the expanding cool flame in a static mixture (red line ABCD in Fig. 6) and the axial propagating cool flame in the counterflow (blue dashed line $A_zB_zC_zD_z$ in Fig. 6). Compared to its counterpart in the axial direction, the cool flame in the radial direction (i.e., z = 0) shows a more unsteady propagation manner due to its high local flame curvature induced by the counterflow.

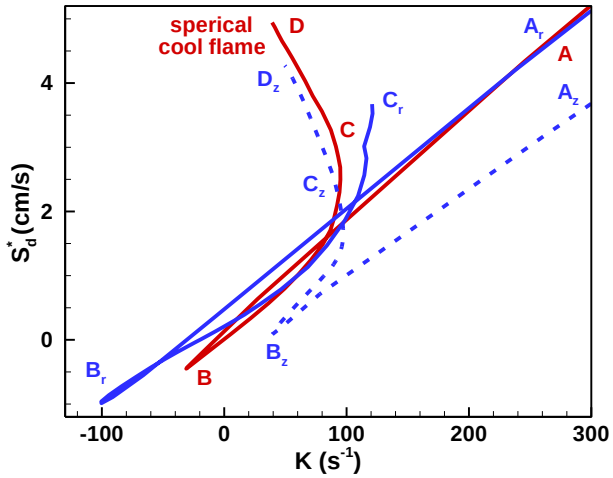

Fig. 6. The variation of density weighted displacement speed S_d^* with local stretch rate K in the axial and radial directions for case A. The blue solid and dashed lines represent the results for cool flame front in the radial (i.e., z = 0) and axial (i.e., r = 0) directions, respectively. The red line represents results for a spherical flame in a static mixture (i.e., a_g = 0 s^{-1}).

3.2 Effects of ignition energy

In this subsection, we study the same global strain rate as in case A, i.e., $a_g = 40$ s^{-1}, but increase the ignition energy. We focus on the thermal runaway process due to LTC and HTC. The effect of varying ignition energies on the maximum HRR is shown in Fig. 7. It is seen that the maximum HRR increases when the ignition energy increases from 0.5 to 0.625 mJ. However, once its peak value is reached, HRR_{max} starts to gradually decline since the ignition energy is not high enough to trigger the LTC thermal runaway. Consequently, no cool flame kernel is formed and ignition fails for case C with $a_g = 40$ s^{-1} and $E_{ign} = 0.625$ mJ. When the ignition energy is increased to $E_{ign} = 0.65$ mJ, the LTC thermal runaway is successfully triggered, leading to the formation of a cool flame kernel whose HRR is around 6×10^8 Jm^{-3}s^{-1}. However, Fig. 7 shows that HRR_{max} starts to decrease at $t = 7.5$ ms. This is because the cool flame kernel gradually quenches under the influence of the stretch rate (similar to case D shown in Fig. 2). Further increasing the ignition energy to $E_{ign} = 0.825$ mJ (corresponding to case A), the cool flame can be stabilized in the counterflow as discussed in sub-section 3.1. This specific ignition energy corresponds to the MIE for the cool flame at the global strain rate of $a_g = 40$ s^{-1}. For $0.825 \leq E_{ign} \leq 1.2$ mJ, the ignition energy is not high enough to induce the HTC thermal runaway and thereby only the cool flame can be observed. When the ignition energy is further increased to $E_{ign} = 1.25$ mJ, HRR_{max} is in the order of 10^{11} Jm^{-3}s^{-1}, indicating that the HTC thermal runaway is triggered, and a hot flame kernel is formed (corresponding to case B shown in Fig. 2). The animations of heat release rate contours for cases B and C are provided in the Supplementary Material. It is noted that since the time scale of the thermal runaway (around 1 ms) is much smaller than the characteristic time scale of the flow (above 10 ms for $a_g < 100$ s^{-1}), the ignition energy required to trigger LTC and HTC thermal runaway is almost independent of the strain rate.

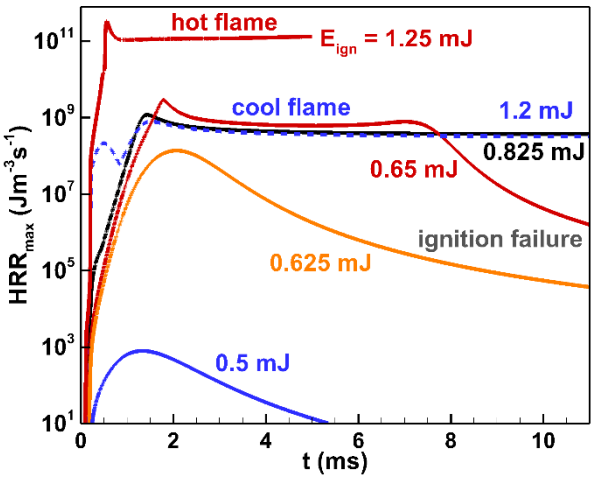

Fig. 7. Temporal evolution of maximum heat release rate, HRR_{max}, for different ignition energies with a fixed global strain rate of $a_g = 40$ s^{-1}. The black solid line with $E_{ign} = 0.825$ mJ corresponds to case A.

The thermal runaway process is similar to the 0D homogeneous ignition characterized by an ignition delay time, τ_{ig}, for each initial temperature. The only difference is that the temperature of the ignition kernel decreases continuously due to heat losses to the surrounding mixture [35]. The time scale for heat conduction is around τ_α = 1 ms according to the relationship, $\tau_\alpha = (R_{ign})^2/\alpha$, where α is the thermal diffusivity of the mixture. When $\tau_{ig} < \tau_\alpha$, a successful thermal runaway can be achieved. The ignition delay time (calculated for the 0D homogeneous ignition process instead of the 2D ignition process) of the stoichiometric DME/air mixture for different temperature ranges at 5 atm is displayed in Fig. 8. For a temperature below 750 K, the ignition delay time is so large that the temperature drops before the thermal runaway can occur. In the temperature range from 750 to 850 K, the delay time for the first-stage ignition is small enough so that the LTC thermal runaway might occur. When the temperature further increases to 850~1150 K, the LTC disappears and the global ignition delay time is too large and the HTC thermal runaway will not occur. For T > 1150 K, the ignition delay time is small enough so that HTC thermal runaway can happen. Therefore, with a suitable ignition energy, either LTC or HTC thermal runaway can occur in the ignition kernel.

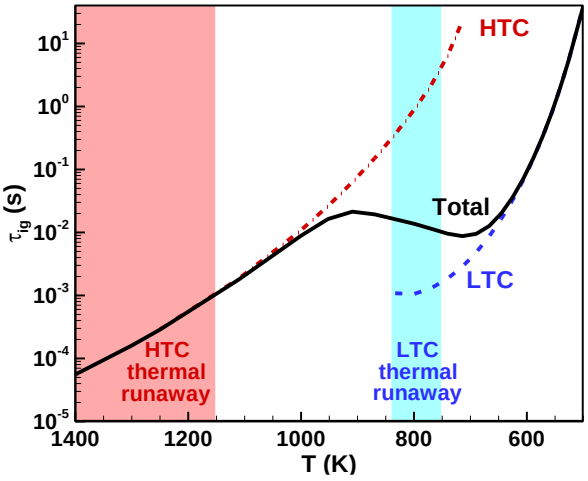

Fig. 8. The ignition delay time for the stoichiometric DME/air mixture at P = 5 atm, which is calculated for the 0D homogeneous ignition process instead of the 2D ignition process. The blue dashed line represents the first-stage ignition delay time, the black solid line represents the total ignition delay time, and the red dashed line represents the ignition delay time predicted by HTC (i.e., the LTC is deleted from the chemistry model).

Figure 9 illustrates the LTC and HTC thermal runaway occurring in cases A and B, respectively. For the LTC thermal runaway in Fig. 9(a), the heat release rate increases during $0 \le t \le 1.3$ ms and it peaks in the region with the temperature corresponding to the lowest first-stage ignition delay time (~800 K according to Fig. 8). Due to the small heat release from LTC, there is no sudden temperature rise after the LTC thermal runaway. The highest temperature remains to be around 800 K when the

cool flame propagates to z = 0.6 mm at t = 85 ms. For case B with a relatively high ignition energy, Fig. 9(b) shows that after ignition energy deposition, the temperature at the center of the ignition kernel is close to 1300 K. During $0 \le t \le 0.52$ ms, the heat release rate continuously increases and exhibits two distinct peaks corresponding to the LTC for $T \approx 800$ K and HTC for $T > 1300$ K. This is consistent with the ignition delay time shown in Fig. 8. After HTC thermal runaway completes, a hot flame kernel is formed, resulting in a rapid rise in the central temperature. The hot flame kernel propagates outwardly and merges with the LTC reaction zone at t=0.58 ms. Consequently, only the hot flame is successfully ignited, and no cool flame can be observed.

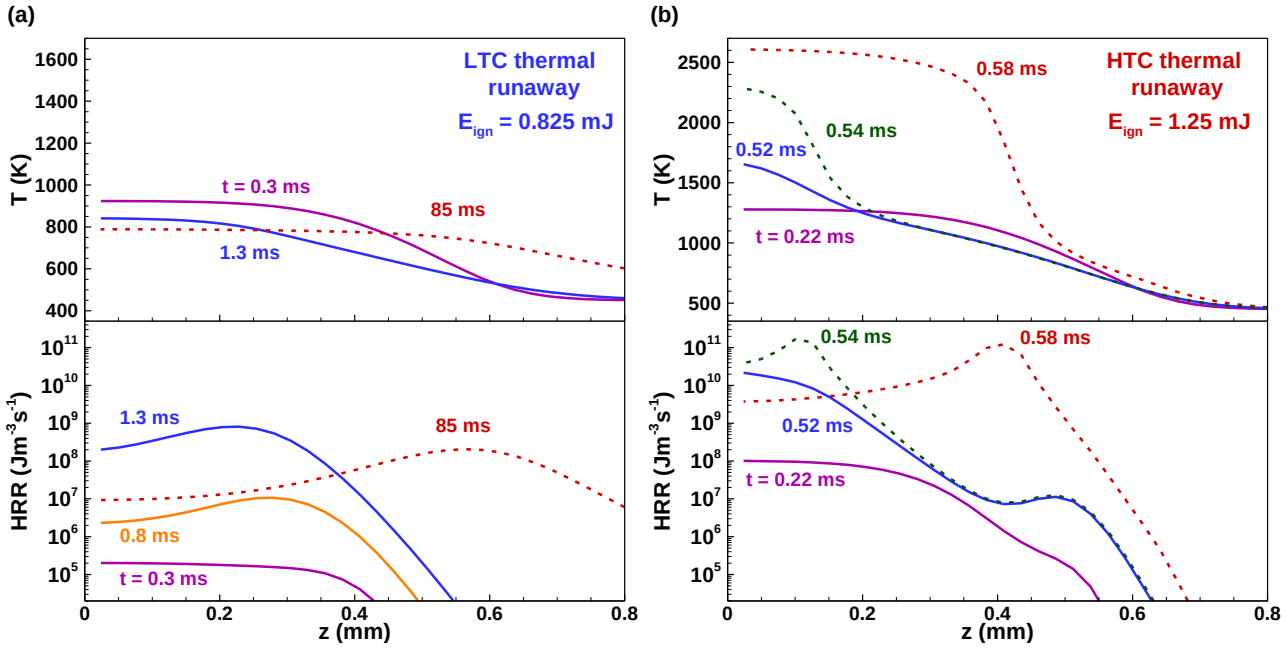

Fig. 9. Evolution of temperature and heat release rate profiles along the symmetry axis (i.e., r = 0) for a_g=40 s^{-1}: (a) case A with E_{ign} = 0.825 mJ, LTC thermal runaway; (b) case B with E_{ign} = 1.25 mJ, HTC thermal runaway.

3.3 Effects of strain rate

In this subsection, we fix the ignition energy to be the same as that in case A, i.e., E_{ign} = 0.825 mJ, but consider different global strain rates. The strain rate affects the cool flame ignition in two ways: (1) it couples with the preferential diffusion between heat and mass (characterized by the Lewis number) and affects the local flame strength; (2) it determines the residence time of intermediate products from the cool flame and thereby affects the transition from cool flame to hot flame.

Figure 10 shows the change of the MIE with global strain rate for both cool and hot flames. It is noted that the red line indicates the MIE for immediate ignition of a hot flame without a cool flame. The MIE is calculated by the bisection method with an error below 0.0125 mJ. For relatively low

strain rates shown in Fig. 10, the MIE for the cool flame increases monotonically, while the MIE for the hot flame remains nearly constant. This is because the cool flame is relatively weaker and more sensitive to the strain rate than the hot flame. Moreover, the successful ignition of the hot flame merely requires the occurrence of an HTC thermal runaway. The time scale in subsection 3.2 indicates that the ignition energy required for an HTC thermal runaway is almost independent of the strain rate. Therefore, the MIE for the hot flame is almost constant for a_g =120 s^{-1} as shown in Fig. 10. In Fig. 10, the MIE for cool flame is close to that of the hot flame at the intersection of the two curves. This corresponds to the critical strain rate, $a_{g,e}$ = 110 s^{-1}, beyond which the cool flame cannot be observed since the hot flame consumes the reactants before the cool flame appears (see Fig. 9b).

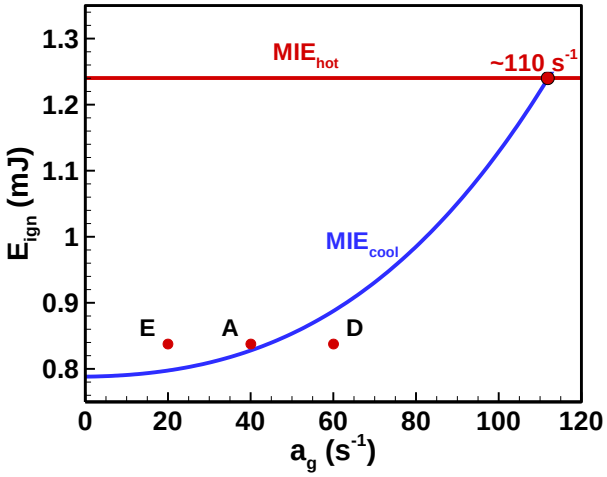

Fig. 10. Change of the minimum ignition energy for cool and hot flames with global strain rate.

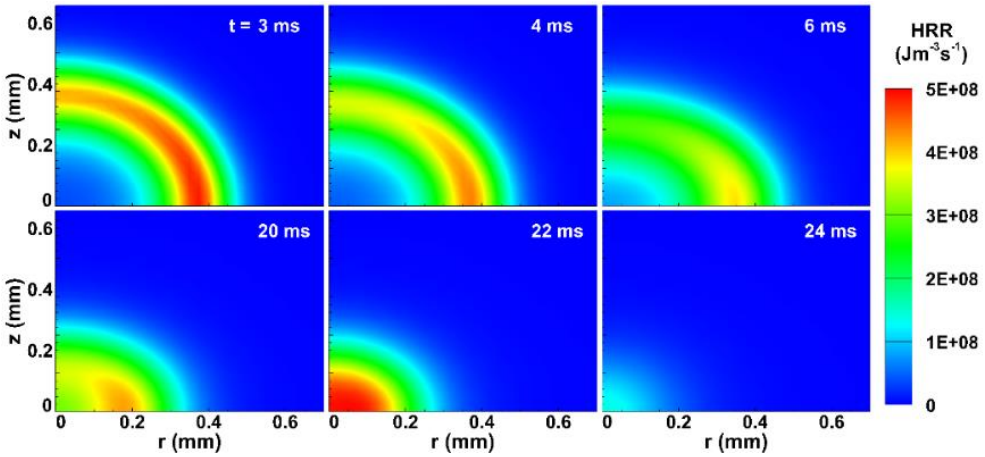

Fig. 11. Temporal evolution of heat release rate during the cool flame ignition and quenching in case D with a_g=60 s^{-1} and E_{ign}=0.825 mJ. An animation is provided in the Supplementary Material.

Compared to case A a_g = 40 s^{-1}, case D has a higher strain rate of a_g = 60 s^{-1}. Figure 11 shows that the cool flame kernel is formed at t=3 ms. At a larger strain rate, the cool flame front experiences a larger aerodynamic stretch rate in the axial direction and larger curvature in the radial direction,

both enlarging the local stretch rate K. Due to the negative correlation between flame speed and stretch rate (see line CD in Fig. 6), the cool flame propagation slows down. Consequently, Fig. 11 shows that the cool flame kernel gradually weakens and quenches during $4 \le t \le 24$ ms. The MIE for $a_g = 40$ s^{-1} is 0.875 mJ, which is higher than E_{ign}=0.825 mJ for case D.

When the global strain rate is reduced from $a_g = 40$ s^{-1} in case A to $a_g = 20$ s^{-1} in case E, both cool flame and hot flame can be observed simultaneously. This is because at lower strain rate, the intermediate products from cool flame have a longer residence time to trigger the HTC thermal runaway. Figure 13 shows that first the cool flame is ignited and propagates outward. Then at t = 106.5 ms, the HTC thermal runaway starts to occur around the stagnation point. Subsequently, a hot flame kernel is formed at around t = 107.1 ms. A double flame structure including a hot flame following the leading cool flame is observed afterwards. Note that the HRR for the cool flame (~6×10^8 Jm^{-3}s^{-1}) is about two-order lower than that for the hot flame (~10^{11} Jm^{-3}s^{-1}). The hot flame has a much higher flame speed than the cool flame, and thereby it eventually catches up and merges with the cool flame. A similar observation was reported by Zhang et al. [14] for the cool flame ignition in a static mixture.

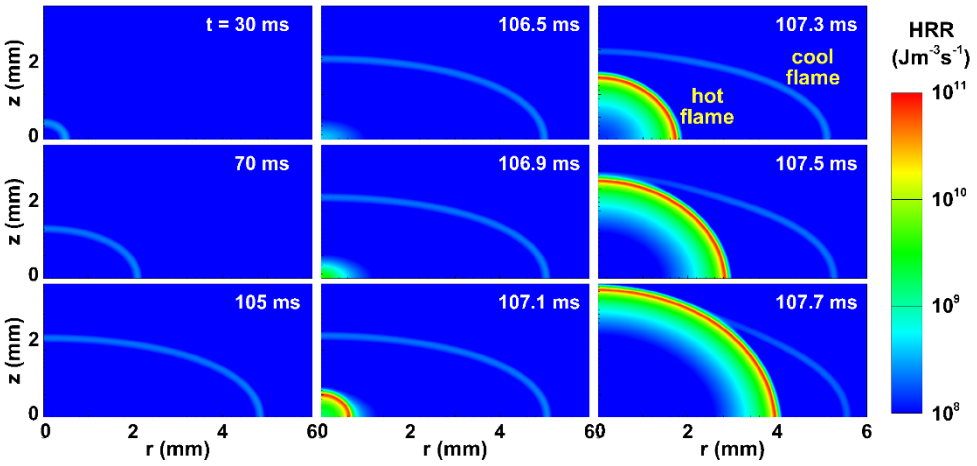

Fig. 12. Temporal evolution of heat release rate during the cool flame ignition and propagation as well as the transition from cool flame to hot flame in case E with a_g=20 s^{-1} and E_{ign}=0.825 mJ. An animation is provided in the Supplementary Material.

Figure 13 further illustrates the double flame structure. The cool flame structure near r = 5 mm is similar to the steady cool flame structure for case A, which is shown in Fig. 4. After the cool flame front, the fuel is partially consumed and the intermediate species such as CH_2O and H_2O_2 are produced. The hot flame front is located around r = 1.7 mm, after which the fuel is completely consumed and the intermediate species are converted into CO_2 and H_2O. The temperature increases from 450 K to around 800 K and 2300 K after the cool and hot flame fronts, respectively.

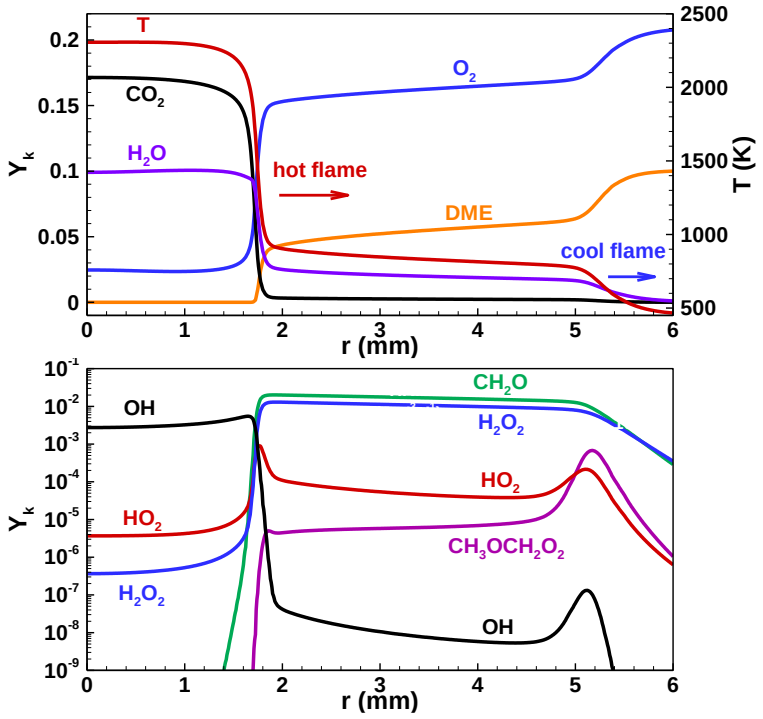

Fig. 13. Double flame structure along the stagnation plane (i.e., z=0) at t=107.3 ms for case E.

In order to quantitatively characterize the transition from cool flame to hot flame, we introduce the second-stage ignition delay time, τ_2, which is defined as the time required for the occurrence of the hot flame kernel at the stagnation point after ignition energy deposition. Figure 14 shows that τ_2 increases monotonically with the strain rate, a_g. There is a critical strain rate, $a_{g,t}$ = 36 s^{-1}, beyond which the second-stage ignition delay time approaches infinity, indicating that no hot flame shall appear. Moreover, Fig. 15 demonstrates that, although increasing the ignition energy can reduce the second-stage ignition delay time, it has a negligible effect on the critical strain rate. With this critical strain rate, the cool flame ignition regime is divided into the "only cool flame" regime and the "double flame" regime.

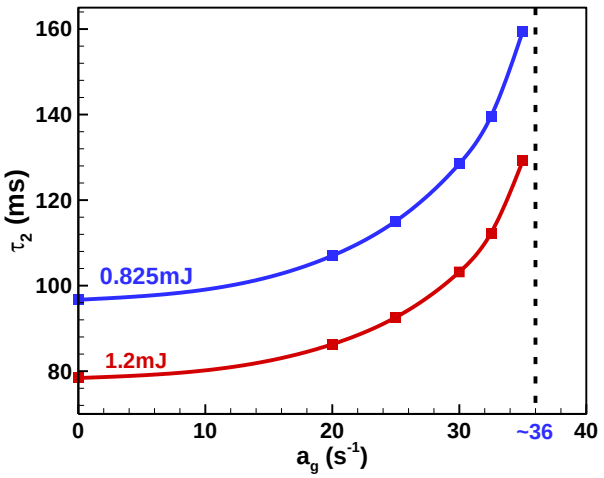

Fig. 14. Change of the second-stage ignition delay time τ_2 with global strain rate for E_{ign} = 0.825 mJ

and E_{ign} = 1.2 mJ. Note that τ_2 is calculated for the 2D ignition process instead of the 0D homogeneous ignition process.

To confirm and interpret the critical strain rate, $a_{g,t}$ = 36 s^{-1} from the 2D simulation, we conduct simulations for a 1D counterflow flame using the in-house Universal Laminar Flame (ULF) solver [36]. The change of the flame temperature with the global strain rate is shown in Fig. 15. The turning points and multiple solutions are calculated using the flame-controlling continuation method [37]. Instead of treating the strain rate as a prescribed parameter, the value of a flame scalar at a specific location is employed as an internal boundary condition, and thereby a continuous mapping of the relationship between the flame response and strain rate is achieved. The solid red and blue branches represent a stable cool flame and hot flame, respectively. The dashed lines correspond to unstable flame branches. This allows us to determine three critical strain rates: the hot flame extinction (HFE) strain rate at $a_{g,HFE}$ = 15525 s^{-1}, the cool flame extinction (CFE) strain rate at $a_{g,CFE}$ = 224 s^{-1}, and the high-temperature ignition strain rate (HTI) at $a_{g,HTI}$ = 42 s^{-1}. The temperature of the hot flame is generally above 1700 K, and it decreases with increasing strain rate until the extinction limit is reached. The cool flame exhibits a similar behavior and its temperature decreases from 900 K to 700 K as the strain rate increases. Note that the extinction strain rate for the cool flame, $a_{g,\,CFE}$ = 224 s^{-1}, is significantly lower than that of the hot flame, $a_{g,\,HFE}$ = 15525 s^{-1}.

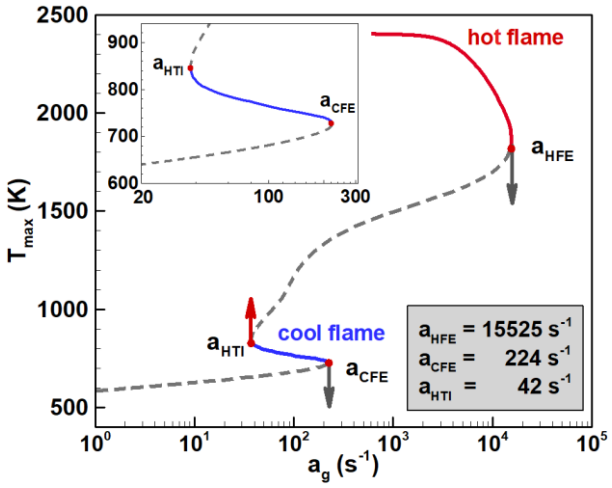

Fig. 15 Change of maximum flame temperature T_{max} with global strain rate a_g in 1D counterflow of a stoichiometric DME/air mixture at T_u = 450 K and P = 5 atm.

We observe that the cool flame extinction strain rate, $a_{g,CFE}$ = 224 s^{-1}, from the 1D counterflow flame calculation is much larger than the critical strain rate, $a_{g,e}$ = 110 s^{-1}, shown in Fig. 11. This is because 1D counterflow flame calculation only considers steady flame, while 2D simulation

considers the transient ignition kernel development and propagation processes. The energy deposition in a small region can result in excessively high temperature, which easily induces HTC thermal runaway and hot flame kernel. The hot flame kernel expands, preventing the appearance of the cool flame (see Fig. 9b and related discussion). Figure 15 indicates that a steady cool flame cannot be observed for strain rates below $a_{g,\mathrm{HTI}} = 42\ \mathrm{s}^{-1}$. This value is close to the critical strain rate shown in Fig. 14, $a_{g,t} = 36\ \mathrm{s}^{-1}$, below which the transition from cool flame to hot flame always occurs.

3.4 The ignition regimes

The results in the previous subsections are integrated into an ignition regime diagram in terms of ignition energy and strain rate shown in Fig. 16. Four regimes are identified, and they include the cases A~E discussed above. In regime I, a cool flame is successfully ignited and finally a steady, twin, premixed, cool flame develops in the counterflow (see case A). There is no transition from a cool flame to a hot flame in regime I. In regime II, a hot flame is ignited and no cool flame appears during the ignition process (see case B). In regime III, ignition fails due to one of the two possible scenarios: (1) the ignition energy is too low to induce the LTC thermal runaway as in case C; (2) the cool flame kernel is not strong enough to propagate outward in a self-sustained manner after LTC thermal runaway (i.e. Case D). In regime IV, with a relatively low strain rate, a cool flame is first ignited, and then a hot flame develops from the stagnation point. The hot flame catches up and merges with the leading cool flame. Finally, a steady, twin, premixed, hot flame develops in the counterflow (see Case E).

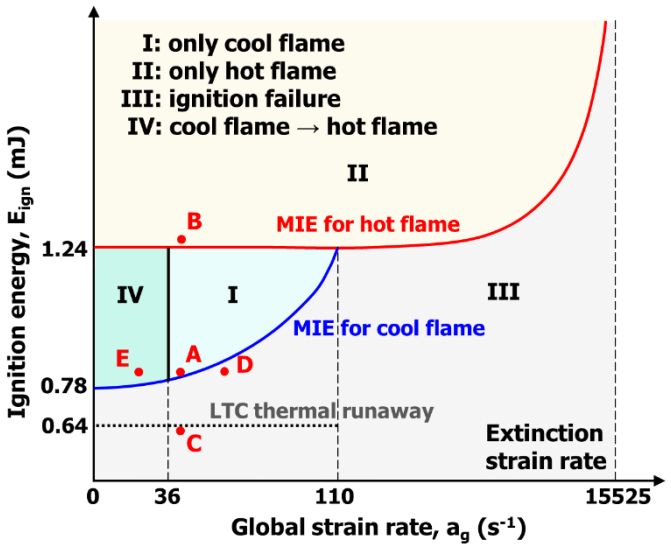

Fig. 16 Ignition regime diagram for a stoichiometric DME/air mixture at 450 K and 5 atm in the axisymmetric counterflow. The values of a_g and E_{ign} for cases A~E are shown in Fig. 2.

Consistent with the regime diagram, Fig. 17 summarizes the ignition kernel evolution for

different ignition energies and strain rates including the five typical cases, A~E. It is seen that the ignition energy mainly determines whether LTC/HTC thermal runaway occurs, while the strain rate mainly determines flame kernel quenching and transition from cool flame to hot flame.

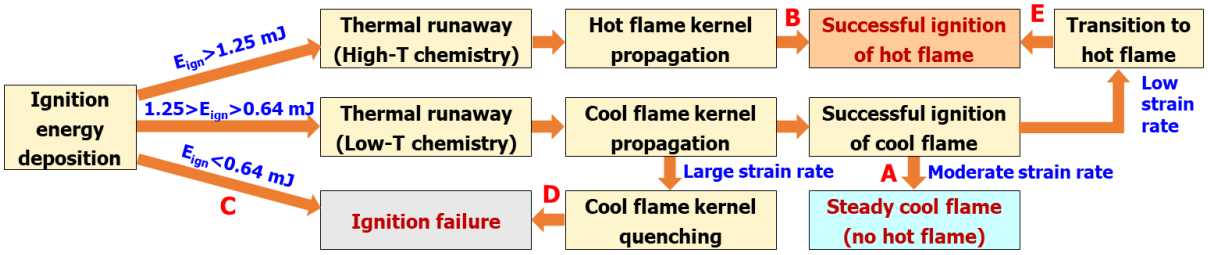

Fig.17 Evolution of ignition kernel under different ignition energies and strain rates. Case A is in ignition regime I, case B in regime II, cases C and D in regime III, and case E in regime IV.

4 Conclusions

Two-dimensional transient simulations are conducted for the forced ignition of cool and hot flames in a laminar counterflow of premixed DME/air. Different ignition energies and strain rates are considered, and their influences on LTC and HTC thermal runaway, cool and hot flame kernel development, and the transition from cool flame to hot flame are assessed. An ignition regime diagram in terms of ignition energy and strain rate (see Fig. 16) is proposed, in which four ignition regimes are identified: (I) only cool flame, (II) only hot flame, (III) ignition failure, and (IV) transition from cool flame to hot flame. Cool flame ignition and hot flame ignition can be achieved through suitable ignition energy deposition at the stagnation point. At low strain rates, the residence time is long enough for the second-stage ignition occurring in the products of the cool flame, and thereby a hot flame appears and eventually merges with the leading cool flame. At intermediate strain rates, the residence time is insufficient for the second-stage ignition to occur and thereby a cool flame appears only. At large strain rates, the cool flame kernel can be quenched, resulting in ignition failure. The findings suggest that the ignition energy primarily determines the occurrence of LTC/HTC thermal runaway, whereas the strain rate primarily governs flame kernel quenching and the transition from cool flame to hot flame.

This work demonstrates that a counterflow has a strong impact on the ignition of a premixed cool flame and on its subsequent transition to a hot flame. As an extension of this work, it would be interesting to investigate cool flame ignition in a turbulent flow. Besides, only stoichiometric mixture is considered here. Fuel-lean and fuel-rich mixtures with different effective Lewis number need to be considered in future works.

Acknowledgements

This work was jointly funded by NSFC, China (project numbers 521760965 and 51861135309) and DFG, German (project numbers 411275182 and 237267381), the Space Application System of China Manned Space Program, and the Fundamental Research Funds for the Central Universities, Peking University. We thank Drs. Thorsten Zirwes, Feichi Zhang, and Henning Bockhorn at Karlsruhe Institute of Technology for providing us their EBI-DNS code and Mr. Felix Rong at Technical University of Darmstadt for providing results in Fig. 15.

Supplementary material

Five animations for the temporal evolution of heat release rate distributions for cases A, B, C, D, and E are provided.

References

[1] H. Davy, International Journal of Heat and Mass Transfer, Phil. Trans. R. Soc 107 (1817) 77–85.

[2] W.H. Perkin, Some observations on the luminous incomplete combustion of ether and other organic bodies, J. Chem. Soc. Trans. 41 (1882) 363-367.

[3] F. Battin-Leclerc, Detailed chemical kinetic models for the low-temperature combustion of hydrocarbons with application to gasoline and diesel fuel surrogates, Prog. Energy Combust. Sci. 34 (2008) 440-498.

[4] H.K. Ciezki, G. Adomeit, Shock-tube investigation of self-ignition of n-heptane-air mixtures under engine relevant conditions, Combust. Flame 93 (1993) 421-433.

[5] Y. Ju, C.B. Reuter, O.R. Yehia, T.I. Farouk, S.H. Won, Dynamics of cool flames, Prog. Energy Combust. Sci. 75 (2019) 100787.

[6] Y. Ju, Understanding cool flames and warm flames, Proc. Combust. Inst. 38 (2021) 83-119.

[7] V. Nayagam, D.L. Dietrich, P.V. Ferkul, M.C. Hicks, F.A. Williams, Can cool flames support quasi-steady alkane droplet burning?, Combust. Flame 159 (2012) 3583-3588.

[8] M. Foster, H. Pearlman, Cool flames at terrestrial, partial, and near-zero gravity, Combust. Flame 147 (2006) 108-117.

[9] H. Pearlman, Low-temperature oxidation reactions and cool flames at earth and reduced gravity, Combust. Flame 121 (2000) 390-393.

[10] C.B. Reuter, S.H. Won, Y. Ju, Experimental study of the dynamics and structure of self-sustaining premixed cool flames using a counterflow burner, Combust. Flame 166 (2016) 125-132.

[11] P. Zhao, W. Liang, S. Deng, C.K. Law, Initiation and propagation of laminar premixed cool

flames, Fuel 166 (2016) 477-487.

[12] S.H. Won, B. Jiang, P. Diévart, C.H. Sohn, Y. Ju, Self-sustaining n-heptane cool diffusion flames activated by ozone, Proc. Combust. Inst. 35 (2015) 881-888.

[13] M. Hori, A. Yamamoto, H. Nakamura, T. Tezuka, S. Hasegawa, K. Maruta, Study on octane number dependence of PRF/air weak flames at 1–5 atm in a micro flow reactor with a controlled temperature profile, Combust. Flame 159 (2012) 959-967.

[14] W. Zhang, M. Faqih, X. Gou, Z. Chen, Numerical study on the transient evolution of a premixed cool flame, Combust. Flame 187 (2018) 129–136.

[15] Q. Yang, P. Zhao, Minimum ignition energy and propagation dynamics of laminar premixed cool flames, Proc. Combust. Inst. 38 (2021) 2315-2322.

[16] Y. Wang, H. Zhang, T. Zirwes, F. Zhang, H. Bockhorn, Z. Chen, Ignition of dimethyl ether/air mixtures by hot particles: Impact of low temperature chemical reactions, Proc. Combust. Inst. 38 (2021) 2459-2466.

[17] Y. Wang, W. Han, T. Zirwes, F. Zhang, H. Bockhorn, Z. Chen, Effects of low-temperature chemical reactions on ignition kernel development and flame propagation in a DME-air mixing layer, Proc. Combust. Inst. 39 (2023) 1515-1524.

[18] M. BAUM, T. POINSOT, Effects of Mean Flow on Premixed Flame Ignition, Combust. Sci. Technol. 106 (1995) 19-39.

[19] J.-L. Beduneau, B. Kim, L. Zimmer, Y. Ikeda, Measurements of minimum ignition energy in premixed laminar methane/air flow by using laser induced spark, Combust. Flame 132 (2003) 653-665.

[20] S. Xie, X. Chen, H. Böttler, A. Scholtissek, C. Hasse, Z. Chen, Forced Ignition of a Rich Hydrogen/Air Mixture in a Laminar Counterflow: A Computational Study, Flow Turbul. Combust. 110 (2023) 441-456.

[21] S.S. Shy, Spark ignition transitions in premixed turbulent combustion, Prog. Energy Combust. Sci. 98 (2023) 101099.

[22] X. Chen, S. Xie, H. Böttler, A. Scholtissek, W. Han, D. Yu, C. Hasse, Z. Chen, Effects of electrodes and imposed flow on forced ignition in laminar premixed hydrogen/air mixtures with large Lewis number, Proc. Combust. Inst. 39 (2023) 1967-1976.

[23] K. Seshadri, F.A. Williams, Laminar flow between parallel plates with injection of a reactant at high reynolds number, Int. J. Heat Mass Transfer 21 (1978) 251-253.

[24] A. Frendi, M. Sibulkin, Dependence of Minimum Ignition Energy on Ignition Parameters, Combust. Sci. Technol. 73 (1990) 395-413.

[25] T. Zirwes, F. Zhang, P. Habisreuther, M. Hansinger, H. Bockhorn, M. Pfitzner, D. Trimis, Quasi-

DNS Dataset of a Piloted Flame with Inhomogeneous Inlet Conditions, Flow Turbul. Combust. 104 (2020) 997-1027.

[26] T. Zirwes, F. Zhang, J.A. Denev, P. Habisreuther, H. Bockhorn, Automated Code Generation for Maximizing Performance of Detailed Chemistry Calculations in OpenFOAM, in: W.E. Nagel, D.H. Kröner, M.M. Resch (Eds.) High Performance Computing in Science and Engineering ' 17, Springer International Publishing, Cham, 2018, pp. 189-204.

[27] T. Zirwes, M. Sontheimer, F. Zhang, A. Abdelsamie, F.E.H. Pérez, O.T. Stein, H.G. Im, A. Kronenburg, H. Bockhorn, Assessment of Numerical Accuracy and Parallel Performance of OpenFOAM and its Reacting Flow Extension EBIdnsFoam, Flow Turbul. Combust., (2023).

[28] X. Chen, Y. Wang, T. Zirwes, F. Zhang, H. Bockhorn, Z. Chen, Heat Release Rate Markers for Highly Stretched Premixed CH4/Air and CH4/H2/Air Flames, Energ. Fuel 35 (2021) 13349-13359.

[29] F. Zhang, T. Zirwes, Y. Wang, Z. Chen, H. Bockhorn, D. Trimis, D. Stapf, Dynamics of Premixed Hydrogen/Air Flames in Unsteady Flow, Phys. Fluids 34 (2022) 085121.

[30] A. Bhagatwala, Z. Luo, H. Shen, J.A. Sutton, T. Lu, J.H. Chen, Numerical and experimental investigation of turbulent DME jet flames, Proc. Combust. Inst. 35 (2015) 1157-1166.

[31] J.H. Chen, H.G. Im, Correlation of flame speed with stretch in turbulent premixed methane/air flames, Symp. (Int.) Combust. 27 (1998) 819-826.

[32] C.K. Law, Combustion Physics, Cambridge University Press, Cambridge, 2006.

[33] Z. Chen, M.P. Burke, Y. Ju, Effects of Lewis number and ignition energy on the determination of laminar flame speed using propagating spherical flames, Proc. Combust. Inst. 32 (2009) 1253-1260.

[34] H.H. Kim, S.H. Won, J. Santner, Z. Chen, Y. Ju, Measurements of the critical initiation radius and unsteady propagation of n-decane/air premixed flames, Proc. Combust. Inst. 34 (2013) 929-936.

[35] D. Yu, X. Chen, Z. Chen, Analysis on ignition kernel formation in a quiescent mixture: Different characteristic time scales and critical heating powers, Combust. Flame 245 (2022) 112336.

[36] A. Zschutschke, D. Messig, A. Scholtissek, C. Hasse, Universal Laminar Flame Solver (ULF), Figshare Poster, 2017.

[37] M. Nishioka, C.K. Law, T. Takeno, A flame-controlling continuation method for generating S-curve responses with detailed chemistry, Combust. Flame 104 (1996) 328-342.